Empirical bifurcation analysis of optical pattern formation

R. Neubecker* and E. Benkler
Institute of Applied Physics, Darmstadt University of Technology, Hochschulstrasse 6, 64289 Darmstadt, Germany
(Received 12 September 2001; published 18 June 2002)

The experimental characterization of pattern forming bifurcations is difficult, since the unstable solutions are generally not accessible in experiments. In nonlinear optics, a novel control scheme allows one to select and stabilize generic patterns and thus to track these solutions in parameter space. This Fourier space scheme is applied to a single-feedback system and the amplitudes of roll, square and hexagon patterns are determined experimentally. Even though the bifurcation is imperfect, the coefficients of a prototype amplitude equation are recovered. The coefficients show satisfactory agreement with theory and with numerical simulations, which are performed for comparison. The simulations also clarify the origin of the imperfect bifurcation in the experiment: boundaries and speckles appear to have an unexpected strong influence.

DOI: 10.1103/PhysRevE.65.066206 PACS number(s): 89.75.Kd, 05.45.Gg, 42.60.Jf, 42.65.Sf

I. INTRODUCTION

The spontaneous formation of spatial patterns is investigated in many fields of physics, and other disciplines such as chemistry and biology [1]. Nonlinear optical systems exhibit a wide variety of such self-organization effects as well, which in this area have been examined systematically in the last decade [2]. Though optical systems are very different from the classical pattern forming systems regarding their microscopic physics, the macroscopic phenomena are surprisingly similar.

One of the main aspects in pattern formation is the analysis of the first bifurcation, where out of the uniform state a number of new stable and also unstable solutions evolve. The investigation of this bifurcation is, in general, limited to theoretical approaches. Experimentally, only stable solutions are observable, hiding possible coexisting unstable states. In order to access unstable states, one has to apply a kind of control. This control must on one hand allow one to select particular states out of the set of coexisting solutions. On the other hand, the selected state must be stabilized, in case it is unstable. Such a scheme should, of course, not alter the system properties—apart from the stability of the solutions.

With the success of the concepts to control temporal chaos, there have been attempts to extend this idea to spatially extended systems [3–6]. A first simple step was to consider coupled maps or networks of nonlinear oscillators. For continuous systems, often, the control has been applied in a global, spatially uniform way or by modulation of a single parameter. More elaborate schemes consider a local control at a finite number of control sites in space. The underlying general problem, in particular for experiments, is that one needs to manipulate physical quantities in time and space. This task is difficult if the corresponding quantities are, for instance, heat, concentration of chemical reactants, or flow fields. Furthermore, the spatially distributed control signal must be derived in time, which depending on the relevant time constants can be difficult. As a consequence, the majority of the work published so far considers theoretical aspects and numerical simulations. Experiments on continuous systems are often restricted to a single spatial dimension. In this report, we will present experimental control on a two-dimensional system. The control signal is not only derived from the full spatial distribution of the system state, but itself is also spatially continuous. Moreover, the control works in real time.

Optics opens new access to the control of extended systems, offering a number of advantages. The possibility to superpose light waves makes it easy to inject external, spatially and temporally modulated (control) signals into a given system. Furthermore, the spatial Fourier transformation capabilities of simple lenses can allow a high-speed derivation of the spatial control signal distribution. Some of the advantages of optics can be made use of in other systems, e.g., when the nonlinear process is photosensitive [4].

To clarify the notation, we would like to stress that we use the terminus *control* for schemes where the intention is to stabilize unstable system states of the unaffected system (*target states*). In particular, the applied control signal should be derived from the system state and the control signal should vanish, when the target state is reached. This is in contrast to *forced* systems, where an external, independent signal is applied—an approach that alters the systems states.

Here, we will make use of a Fourier space control scheme, by which we stabilize different stationary, spatially periodic patterns [7–11]. This scheme makes use of the fact that the spontaneous patterns, which evolve above threshold, consist of a few discrete Fourier modes. In the following, we use the Fourier control as a tool to investigate unstable patterns, which are not accessible otherwise. In particular, the pattern amplitudes are measured, giving an empirical bifurcation diagram. From this diagram, the coefficients of an appropriate prototype amplitude equation are derived. A comparable experimental determination of amplitude equations coefficients has recently been performed for a spatially one-dimensional, fluid-dynamical system [5].

In the remainder of this paper we will first briefly review the nonlinear optical system together with the implementation of the Fourier space control scheme. Section III describes how individual pattern solutions are selected and tracked in parameter space to determine an experimental bi-

*Email address: ralph.neubecker@physik.tu-darmstadt.de

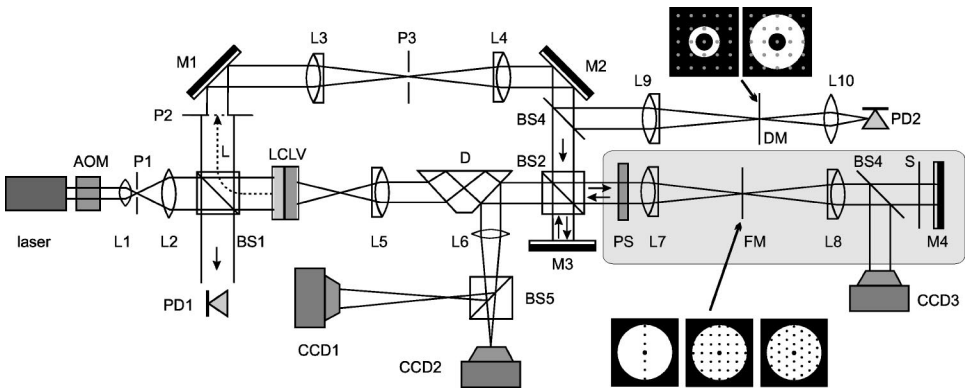

FIG. 1. Schematic drawing of the setup. LCLV, liquid crystal light valve; BS, beam splitters; *M*, mirrors; *L*, lenses. The phase modulated beam, as reflected by the LCLV read side (lhs of LCLV) propagates to the LCLV write side (rhs of LCLV). The control loop is indicated by a gray box. It contains the spatial Fourier filter set up by the lenses $L7$, $L8$ and the mask FM. The appropriate phase of the control wave is set by a Babinet-Soleil phase shifter PS. The control can be deactivated by closing shutter *S*. The optical power in the critical wave number k_c, as selected with the lenses $L9$, $L10$ and the detection mask DM, is measured with the detector PD2. The optical near field (in a plane corresponding to the LCLV write side) and the far field are detected by video cameras (CCD1, CCD2). The control signal is monitored by a camera (CCD3), alternatively by a photodetector.

furcation diagram. In Sec. IV, the corresponding results of numerical simulations are presented and are compared to the experimental findings. In Sec. V, we investigate the different possible causes, which lead to an imperfect bifurcation. The relation between the phase and intensity amplitudes is established in the Appendix. The phase is the variable used in the model, while the intensity is the experimental observable.

II. INTRODUCTION TO THE SYSTEM

A. The nonlinear optical system

The optical nonlinearity is provided by a so-called *liquid crystal light valve* (LCLV), acting as saturable defocusing Kerr-type nonlinearity. The LCLV is a multilayer structure with a read side (liquid crystal layer) and an intensity sensitive write side (photoconductor). The two layers are separated by a dielectric mirror and sandwiched by transparent electrodes to which an ac voltage is applied. According to the local illumination of the photoconductor, the liquid crystal layer locally changes its refractive index [12]. A uniform pump laser beam, reflected by the LCLV read side, acquires a transverse phase shift distribution $\Phi(x,y)$, which is determined by the intensity profile $I_w(x,y)$, incident at the LCLV write side.

In our setup, the phase modulated pump beam is fed back to the write side (see Fig. 1). During propagation through the feedback loop, spatial phase variations are transformed into intensity modulations by means of diffraction. The LCLV then transforms this intensity modulation back to a phase modulation, such closing the feedback loop. As soon as the intensity of the pump beam I_p exceeds a certain threshold, the initially uniform state breaks up: patterns evolve in the transverse cross section of the light wave. At the LCLV read side, these are pure phase patterns, corresponding to intensity patterns at the LCLV write side.

There is a simple physical picture for this pattern formation process: the *Talbot* effect describes the fact that the transverse profile of a spatially periodic wave front reappears after a certain propagation length [13]. A periodic phase profile is transferred into an intensity profile of the same shape after a certain fraction of this so-called *Talbot length*, which depends on the light wavelength and the spatial periodicity of the profile. The spontaneous pattern now selects its own wave number such that, after propagation over the given length in the setup, the resulting intensity profile at the LCLV write side has maximum contrast. Since the Talbot effect originates from diffraction, there is a long range spatial coupling throughout the pattern.

The setup is called *single feedback*, since the modulated wave is fed back to the optical nonlinearity only once, in contrast to resonators with multiple passages of the light wave. Such single-feedback systems recently became quite popular [14–16], because they have a number of advantages, e.g., the clear separation of the two main ingredients for spatial instabilities: diffractional spatial coupling and the nonlinearity. The use of LCLVs as optical nonlinearity has proven to offer great experimental flexibility in various implementations [17]. In particular, it is possible to realize large aspect-ratio patterns even with low laser powers.

The theoretical model for the system used here is composed of two parts: the propagation of the light wave in the feedback loop and the nonlinear response of the LCLV. From the paraxial wave equation, we can derive a formal solution

$$E_w = \exp\left(-i\frac{L}{2k_0}\Delta_\perp\right)E_m = \exp\left(-i\frac{L}{2k_0}\Delta_\perp\right) \times[\exp(-i\Phi)\,E_p], \tag{1}$$

which connects the phase modulated light field E_m at the LCLV read side with the field E_w at the write side. Here, $\Delta_\perp$ is the Laplacian in the transverse coordinates (x,y), L is the diffraction length in the feedback loop, E_p the amplitude of the plane pump wave and $k_0 = 2\pi/\lambda$ its longitudinal wave number.

The LCLV transforms the write intensity distribution I_w

$\sim|E_w|^2$ to a phase distribution via a nonlinear response function $S(I_w)$. Since the dynamical response is slow, in particular with respect to the light round-trip time, a relaxation term with a time constant τ has to be added. Moreover, the spatial resolution of the LCLV is limited, which is considered in a diffusionlike behavior with an effective diffusion length l. All this leads to an equation for the nonlinear phase response

$$\tau\dot{\Phi}+l^2\Delta_\perp\Phi+\Phi=S(I_w), \tag{2a}$$

$$S(I_w)=\Phi_{\max}\left[1-\tanh^2\left(\frac{\kappa_r I_w+1}{\kappa_s I_w+1}\frac{S_0}{V_0}V_{\text{ext}}-\frac{V_{\text{th}}}{V_0}\right)\right]. \tag{2b}$$

The LCLV is characterized by the parameters $\tau\approx 50$ ms, $l=30$ μm, and $\Phi_{\max}=6.02\pi$, $\kappa_r=2.15$ cm$^2/\mu$W, $\kappa_s=1.31$ cm$^2/\mu$W, $S_0/V_0=0.0852$, and $V_{\text{th}}/V_0=0.5521$ for the saturation function. These parameters have been determined in separate measurements. The external ac voltage V_{ext} sets the operation point of the device. In principle, Eq. (1) can be inserted into Eq. (2), leading to a single nonlinear partial differential equation in a scalar real variable $\Phi(x,y,t)$.

A linear stability analysis of this model gives the threshold of pattern formation. In our case, we find a stationary bifurcation to patterns $\Phi(x,y)$, characterized by a single critical wave number k_c. There are also higher unstable wave numbers $k_c^{(n)}$, having higher pump thresholds [16]. For the parameters of the following experiment, we find the theoretical threshold at a pump intensity of $I_{\text{th}}=48.66$ μW/cm^2 and the modulus of the critical wave number to be $k_c=19.15$ 1/mm.

There are three prototype solutions of different symmetries, determined by a single wave number k_c, namely, roll, square, and hexagon patterns. Close to threshold, when resulting harmonics are negligible, these patterns simply read as

$$\Phi=\Phi_0+\hat{\Phi}\sum_{n=1}^{N}\cos(\vec{k}_n\vec{r}+\psi_n),\quad \vec{k}_n=k_c\begin{pmatrix}\cos(2n\pi/N)\\ \sin(2n\pi/N)\end{pmatrix}, \tag{3}$$

with $N=1,2,3$, respectively. The amplitude of these phase profiles is $\hat{\Phi}$, a homogeneous offset is given by Φ_0, and ψ_n are spatial phase shifts.

From experiments and numerical simulations we know that in our case, hexagonal arrangements of bright spots are the dominating pattern just above threshold, while the other solutions are unstable. However, under further increase of the pump intensity, even hexagons soon become unstable and spatiotemporal disorder sets in [18]. Hence, most of the regular pattern solutions are effectively unstable in the largest part of parameter space. The aim of the control will be to make these solutions accessible.

With a perturbation theory, one can go beyond the linear stability analysis and describe the growth of the different regular patterns by so-called amplitude equations [1]. Such an amplitude equation has not yet been derived for the full quantitative model of Eqs. (1) and (2). Up to third order, for the stationary state $\partial/\partial t\,\hat{\Phi}=0$, these equations have the general form

$$a\hat{\Phi}^3+b\hat{\Phi}^2+H=(I_p-I_{\text{th}})\hat{\Phi}. \tag{4}$$

Since we consider perfect patterns, spatial derivatives are not included here. This equation describes a square-root dependence of the amplitude on the reduced stress parameter I_p-I_{th}. In the above form, the parameter $H<0$ accounts for a so-called *imperfect* bifurcation, i.e., a smooth onset of the pattern amplitude. In general, a hexagonal pattern bifurcates subcritically ($b<0$), while squares and rolls bifurcate normally with $b=0$ [1].

In Eq. (4), the coefficients a, b, and H have the dimension of an intensity. In theoretical approaches, where the threshold is known, this equation is mostly given in dimensionless form

$$a'\hat{\Phi}^3+b'\hat{\Phi}^2+H'=(p-1)\hat{\Phi}, \tag{5}$$

with the coefficients divided by the threshold intensity I_{th}, and a dimensionless stress parameter $p=I_p/I_{\text{th}}$.

A nonlinear theory had been performed in [15] for a thin slice of a Kerr medium under single optical feedback. While in the Kerr model the induced phase is proportional to intensity $\Phi\sim I$, in the present system instead, the nonlinearity (2) is saturable. The authors of [15] calculated the amplitudes of hexagon and roll solutions. They find hexagons to be the stable solution, bifurcating subcritically with a rather small hysteresis. The unstable rolls bifurcate normally; squares had not been considered. The coefficients read as [19]

$$\text{Rolls } a'=\chi^2\frac{3\sin\vartheta_{th}-\sin 3\vartheta_{th}}{8\sin\vartheta_{th}},\quad b'=0,$$

$$\text{Hexagons } a'=\chi^2\frac{11\sin\vartheta_{th}-4\sin 2\vartheta_{th}-\sin 3\vartheta_{th}}{8\sin\vartheta_{th}},$$

$$b'=-\chi\frac{1-\cos\vartheta_{th}}{2\sin\vartheta_{th}}, \tag{6}$$

where ϑ_{th} is the solution of $\tan\vartheta_{th}=\vartheta_{th}+\sigma$ and $\sigma=L/(k_0l^2)$ measures the relative strength of diffusion. Our system is in the limit of weak diffusion $\sigma=28.2\gg 1\Rightarrow\vartheta_{th}=1.49\pi$. Setting $\chi=-1$ for the defocusing nonlinearity of the LCLV, we arrive at

$$\text{Rolls } a'=0.4995\approx 1/2,\quad b'=0,$$

$$\text{Hexagons } a'=1.53\approx 3/2,\quad b'=-0.515\approx -1/2, \tag{7}$$

where the approximative values belong to vanishing diffusion $\sigma\to\infty$. When comparing this prediction to our experimental and numerical results, we have to keep in mind that the Kerr model is only an approximation. The amplitude equations coefficients also depend on the higher order terms of the saturable nonlinearity of Eq. (2).

B. Fourier space control

The control scheme follows the idea of a negative feedback regulator, but here, all *signals* are not only time- but also space-dependent fields. The principle is to derive the deviation of the actual system state from a *target state*, chosen beforehand. This deviation is the control signal, which has to be coupled back into the system with a negative sign. Such, all nontarget state contributions are discouraged and the system should move towards the target state. If the target state belongs to the set of solutions, the control signal will naturally vanish asymptotically. In our case, the target states are the above mentioned, spatially periodic patterns, consisting of few spatial Fourier modes.

The terminus *feedback* should not cause confusion at this point, since the underlying system without control has already been denoted as a *single feedback*. The control loop, which is introduced here, represents an additional feedback.

The system state is probed by coupling out a small fraction of the light wave. Optical spatial Fourier filters are ideally suited to derive the control signal: a mask in the Fourier plane between two lenses just blocks all modes of the target pattern. The transmitted residue represents the deviation from the target state, being fed back into the system. Since we consider light waves, an appropriate setting of the relative phases allows us to choose negative interference between the control and the original wave, resulting in the desired negative feedback.

In the model, the Fourier control can simply be included by replacing

$$E_w(x,y) \rightarrow (1 - s\mathcal{F}^{-1}\mathcal{M}\mathcal{F})E_w(x,y) \tag{8}$$

in Eq. (2). The *control strength* $0 \leqslant s \leqslant 1$ determines the maximum amplitude of the control signal, $\mathcal{F}$ stands for the spatial Fourier transform and $\mathcal{M}$ for the Fourier mask. This mask is transmittant for nontarget modes E_{nt}: $\mathcal{F}^{-1}\mathcal{M}\mathcal{F}E_{\mathrm{nt}} = E_{\mathrm{nt}}$ and blocks all target modes E_t. Consequently, if the system is in the target state, the control signal vanishes $\mathcal{M}\mathcal{F}E_t = 0$.

Note that the control signal is continuously distributed in space. The typical spatial resolution of an optical Fourier filter ($\approx 10\ \mu$m) is even smaller than the diffusion length of the LCLV ($l = 30\ \mu$m), which in turn sets the lower bound for the length scales of emerging structures. The passage time of the wave through the control loop is typically some nanoseconds. This is orders of magnitude faster than the time constant of the LCLV ($\tau \approx 50$ ms), determining the time scale of the pattern formation dynamics. Consequently, the control is effectively instantaneous. The situation would become more challenging, when the system time constant is comparable to the transit time of the control loop [6].

We have already shown that the total control power indeed becomes small, when the target state is reached [10]. Moreover, the spatial distribution of the control signal can be recorded by a camera, giving information about what drives the system away from the ideal target state [11].

It should be noted that, in general, there are two states of hexagonal symmetry, one with distinct peaks, one with dips (*honeycombs*). However, the spatial Fourier spectra of these two hexagonal solutions differ only in their phase. For this reason, the simple Fourier control scheme used here, omitting rotations and phase shifts in the Fourier plane [7], cannot select between them. Therefore, the unstable honeycombs are not observed.

The Fourier space control scheme has been proposed and tested numerically in [7]. Simplified versions of this scheme have been implemented experimentally in different nonlinear optical systems. Here, an extra control loop has been omitted by introducing the Fourier filter directly into the system [8,9].

C. Experimental setup

The complete optical setup is shown in Fig. 1. As light source, a linearly polarized, 100-mW-frequency doubled cw Nd:YAG (yttrium aluminum garnet) laser is used. The laser power is controlled by an acousto-optical modulator. The laser beam is cleaned and expanded to about 30 mm diameter (lenses $L1$, $L2$, pinhole $P1$) but only the central 8 mm are used. The optical power of the beam entering the setup is monitored by the photodiode PD1.

The beam is phase modulated and reflected by the LCLV read side and guided back to the write side by several beam splitters and mirrors. The modulated wave propagates free over a distance of $L = 30$ cm between the LCLV and the aperture $P2$. From this plane, the wave front is imaged by the lenses $L3$, $L4$, $L5$ onto the LCLV write side. A rotatable dove prism D is necessary to correct a slight unwanted beam rotation, which can occur due to slight misalignments of the mirrors.

Experimentally, the Fourier control is realized by coupling out a fraction of the wave by the beam splitter BS2. The 4f arrangement of the lenses $L7$ and $L8$ provides a Fourier plane, where the signal can be filtered by inserting a mask FM. The mask is a plane glass plate with a lithographically structured chromium layer. The design of this Fourier mask determines the target state [7,11]. The filtered signal is then reflected by the mirror $M4$, passing the Fourier filter again.

The beam splitter BS2 and the mirrors $M3$, $M4$ form a Michelson interferometer. By appropriate setting of the relative phase of the two interferometer arms, destructive interference is achieved and the control signal is subtracted from the original signal. The control strength s can be set by the reflection ratios of the beam splitters BS2 and BS4 (pellicle), here to $s = 0.4$. The main experimental challenge is to achieve an even interference over the whole beam diameter. This requires minimal wave front distortions in the control loop and good alignment of the optical components.

It has been demonstrated that the stabilization of different target states is possible in parameter regimes, where they are otherwise unstable and experimentally not observable [7,10,11]. Examples of patterns are shown in Fig. 2. In the uncontrolled pattern, we find around 25 spots along the diameter of 8 mm of the active area. This agrees very well with the prediction of the linear stability analysis.

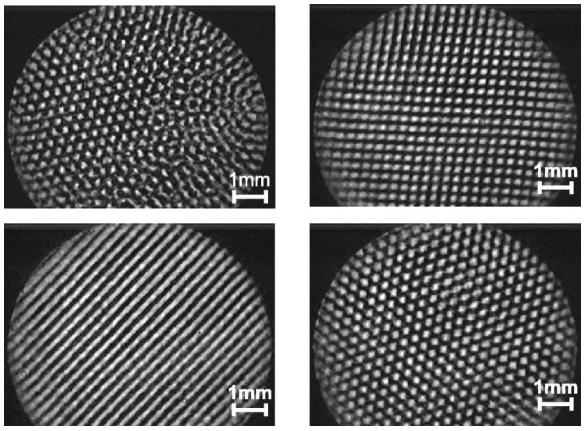

FIG. 2. Typical intensity distributions observed at the LCLV write side for a pump intensity of $I_p = 100\ \mu\mathrm{W/cm^2}$. The uncontrolled state is almost hexagonal (upper panel, lhs). Perfect roll, square, and hexagon patterns form under the action of appropriate control.

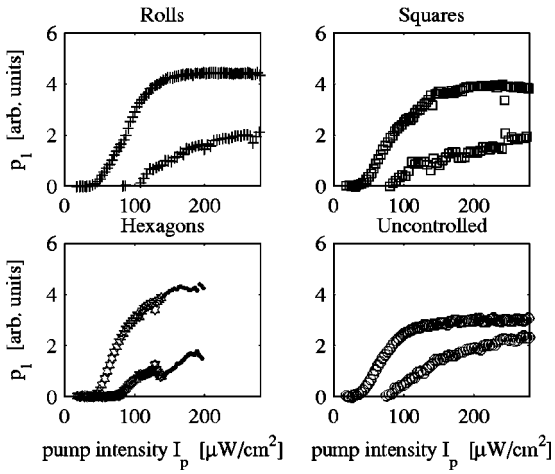

FIG. 3. Experimentally measured relative optical power p_c in the critical wave number (upper curves) and p_h in the harmonics (lower curves).

III. EXPERIMENTAL BIFURCATION ANALYSIS

We will now make use of the control scheme to track the different target states in parameter space. This allows us to measure the corresponding amplitudes even in regimes where these solutions are otherwise unstable. In particular we will be able to characterize the bifurcation from the uniform to the patterned state.

The measurements are carried out with decreasing pump intensity, starting from large values. The main expectation is that for patterns emerging from a normal bifurcation, the recorded optical power should monotonically approach zero at threshold. For hexagons, which bifurcate subcritically, the amplitude should, in the case of a perfect bifurcation, instead remain finite even below threshold, before suddenly falling to zero. Such a hysteresis has previously clearly been detected in another optical single-feedback experiment [9] with sodium vapor as nonlinear medium. Experimentally, it is not simple to detect the amplitudes of the phase patterns $\hat{\Phi}$. We have instead detected the power spectrum of the light wave in the feedback loop. In the Appendix, the relation between the phase and intensity amplitudes of the basic Fourier modes is established, allowing one to reconstruct the phase amplitudes.

The detection is realized by coupling out part of the feedback wave with beam splitter BS4. In the focal plane of lens $L9$, a detection mask DM transmits only wave numbers in the annulus $0.5k_c < |\vec{k}| < 1.2k_c$. The photodiode PD2 detects the total light power P_c in this wave number band. A second measurement is performed with a detection mask that transmits in the range $0.5k_c < |\vec{k}| < 2.1k_c$. The amplitudes in higher wave numbers are determined by subtraction of both measurements.

Recording a scan under systematic variation of the pump intensity is experimentally rather demanding. After setting a certain pump intensity, it is vital that the system comes to rest and the transients die out. In all cases, starting at high values far above the threshold the pump intensity was systematically decreased. The steps between the acquisition of two reading points were $\Delta I_p = -3\ \mu\mathrm{W/cm^2}$. The limited stability of the interferometer required to readjust the phase of the interfering light waves for every reading point.

Figure 3 shows the measured optical power in the critical wave number $p_c = P_c / P_p$, relative to the total pump power P_p, in arbitrary units. For comparison, the case of the uncontrolled, freely running system is shown as well, which of course does not represent the tracking of a particular system state. In the plots, also the relative power in the harmonics p_h is shown.

It was not possible to stabilize the hexagons for pump values larger than $120\ \mu\mathrm{W/cm^2}$. For larger pump values, rolls appeared instead. This can happen for our control scheme, since the two roll modes are a subset of the six hexagon modes. The hexagon-roll transition is also reflected in a distinct dip in the amplitude of the harmonics.

For the square pattern, there is also a change in the solution which is more subtle. A closer look at the patterns reveals that the square patterns are slightly sheared. In the Fourier plane, this corresponds to the fact that the angles between two adjacent modes are not exactly 90°. In the experiment, we see typically a deviation of up to 5°. Consequently, the resulting mixed harmonic as linear combination of the two modes including the smaller angle is larger than $\sqrt{2}k_c$.

A simple explanation is that the next unstable wave number $k_c^{(2)} \approx \sqrt{7/3}k_c$ [15,16] is very close and pulls this mixed harmonic. As we will see later, the transition between pure and sheared squares is observed in the numerical simulations as well. Such sheared squares or *rhomboids* are also a regular pattern solution, since they contain just discrete modes with the critical wave number.

Experimentally, the evolution of sheared squares cannot be prevented completely. The spots on the Fourier mask, blocking the target pattern modes, necessarily have to have a finite diameter [11]. Since the modes of the sheared and the exact square patterns do not differ very much, there is no strict discrimination between exact and sheared squares. A

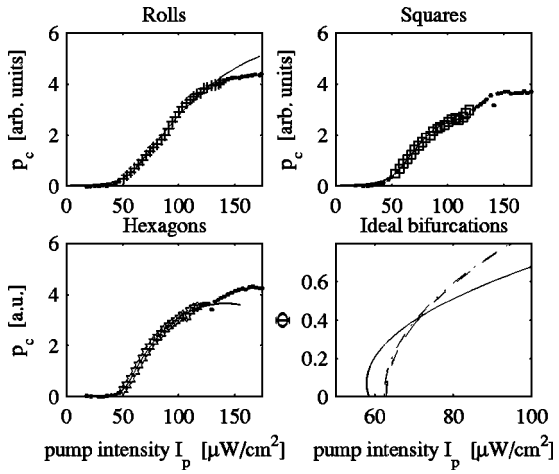

FIG. 4. Fits of the theoretical curve into the measured relative power in the critical mode. The data points included in the fit are indicated by larger markers. The lower rhs plot shows the reconstructed ideal bifurcation diagram $\hat{\Phi}(I_p)$ with $H=0$ (dashed line, rolls; dash-dotted line, squares; solid line, hexagons).

bend in the amplitude of the harmonics may indicate a transition to appear at $I_p \approx 100\ \mu\mathrm{W/cm^2}$.

For high pump intensities, we observe a saturation of the power in the critical wave number. This saturation goes along with the growth of the harmonics. The harmonics play a particular important role for the stability of the square patterns. If they are cut off by the spatial low pass filter ($L3$, $P3$, $L4$ in Fig. 1), we observe the square pattern to decay to the roll solution, which is also compatible with a square target mask.

An important fact is that instead of a sharp onset of pattern formation, we find that all amplitudes grow smoothly from zero. In particular, the subcritical bifurcation, which was expected for the hexagons is not obvious from the measurement and may be hidden by the smooth onset. This so-called *imperfect bifurcation* is well known from other systems, too [1]. It is caused by imperfections, namely, by spatial inhomogeneities. A more detailed discussion about the influence of inhomogeneities will follow in the last section.

We will now reconstruct a bifurcation diagram in the phase amplitudes $\hat{\Phi}(I_p)$ from the measured relative optical power p_c. We assume that, close to threshold, the phase amplitude follows the simple, quadratic dependence of the amplitude equation (4). We use the quantities a, b, H, and I_{th} as fit parameters of a least squares fit, using a simplex direct search algorithm provided by the numerical package MATLAB.

The relation between the relative power in the critical wave number and the phase amplitudes $p_c(\hat{\Phi})$ is derived in the Appendix. The corresponding Eqs. (A4), (A7), and (A11), together with Eq. (A14), cannot be inverted analytically, so that we use a numerical interpolation instead. An additional fit parameter is the scaling of p_c, since this power had not been determined in absolute values. The result of these fits is shown in Fig. 4. From the fitted parameters, we can reconstruct the diagram of a perfect bifurcation by setting $H=0$.

The lower limit of the data points included in the fit interval is chosen such that too small amplitudes with large relative errors are excluded. For the hexagons and the squares, the upper bound is given by their range of existence. In general, the choice of the upper limit has to be a compromise. On one hand, the quadratic approximation Eq. (4) will fail for too large pump intensities. On the other hand, close to threshold the smooth onset of the imperfect bifurcation dominates, hiding the original bifurcation characteristics. The coefficients of the amplitude Eq. (4), found by the fit are displayed in Table I [20].

The coefficients a, b, H, and the threshold I_{th} are given in $\mu\mathrm{W/cm^2}$. These coefficients depend on the chosen pump intensity interval and on the fit start parameters, which limits the reliability. However, the found thresholds are always within a range of $\pm 5\ \mu\mathrm{W/cm^2}$.

The thresholds for the different patterns are very close to each other and are in the order of the theoretical value of $I_{\mathrm{th}}=48.66\ \mu\mathrm{W/cm^2}$, as predicted by the linear stability analysis. The threshold is quite sensitive to some of the LCLV parameters. For instance, a change in the diffusion length l by a few microns already leads to a similar change of the threshold. Hence, the dependence on room temperature may already explain the observed difference between experimental and theoretical threshold. A further possible reason for the deviation is discussed in Sec. V.

The fit also shows that the hexagon solution indeed bifurcates subcritically, but with a very small hysteresis, as predicted by D'Alessandro and Firth [15]. Whereas the roll and square patterns are found to bifurcate normally, as expected. The coefficient H, describing the imperfect bifurcation, is at least in the same order of magnitude for the three measurements, which is quite reasonable. Due to the dependence on the fit interval and the number of coefficients fitted, this fit may not be a rigorous proof. However, the fact that all coefficients have the correct sign and are close to the expected values indicates that the experiment and theory agree.

IV. NUMERICAL SIMULATIONS

For comparison, numerical simulations of the full quantitative model of Eqs. (1) and (2) were carried out. In order to

TABLE I. Amplitude equation coefficients, found by a fit of the experimental data. The values of a, b, H, and I_{th} are given in $\mu\mathrm{W/cm^2}$.

	a	b	I_{th}	H	a'	b'	H'
Rolls	50.0	-0.0003	63.0	-4.54	0.794	-4.2×10^{-6}	-0.0720
Squares	50.3	-0.0004	62.4	-3.20	0.807	-6.4×10^{-6}	-0.0674
Hexagons	114.0	-16.1	58.5	-1.39	1.95	-0.275	-0.238

get as close as possible to the ideal bifurcation characteristic, we here chose periodic boundary conditions and did not include possible inhomogeneities.

The model equations are solved in several steps. In one time step, first, the propagation of the phase modulated pump wave is solved in Fourier space by multiplication of an appropriate phase factor. The resulting field is then transformed back to real space, yielding the intensity distribution at the LCLV write side, from which the nonlinear phase response is computed. Diffusion is included by multiplication of k^2 to the spatial Fourier transform of the observed phase $\Phi(x,y,t+\Delta t)$. It has turned out that a simpler and faster implicit-explicit scheme led to a small error, resulting in a noticeable deviation of the pattern formation threshold.

The simulations were run with a square grid with 256^2 grid points and a pattern aspect ratio of 30. The Fourier control scheme was implemented numerically by attenuating the nontarget modes of the phase modulated light field by a factor $(1-s)$. In general, the control strength $s=0.4$ has been chosen in accordance with the experimental value. In the simulations, it was checked for each value of the pump that the control signal decays. The fact that the average phase change between two integration steps falls below a given low boundary was taken as indication for convergence. From the resulting phase distributions, the different harmonics were extracted in Fourier space by summing over all modes within a given annulus.

For roll and square patterns, it is not a problem to choose the parameters such that the modes of the target pattern exactly match numerical grid points in Fourier space. For hexagons however, this can work only for one of the three modes. Hence, the computed pattern can never be exactly hexagonal. The approximation can be the better, the higher the chosen aspect ratio is. We mention this well-known detail, since it follows that in the simulations a number of nearly hexagonal patterns coexist, which slightly differ from each other in relative angle and modulus of the three modes. The crucial point is that these coexisting patterns also differ in amplitude. Therefore, care has to be taken in the choice of the target pattern modes to match the ideal critical hexagonal pattern as close as possible.

Figure 5 shows the numerically found phase amplitudes in the critical wave number $\Phi_c=\Phi(0.8k_c<k<1.2k_c)$, and in the harmonics $\Phi_h=\Phi(1.2k_c<k)$. Displayed therein are the angular sums over the absolute amplitudes of all modes in these wave number bands. The phase amplitudes $\hat{\Phi}$ of the critical wave number result from a division by the number of modes. The corresponding relative optical powers, which have been the experimentally accessible quantity, are also shown in Fig. 5.

For very high values of the pump, the numerical Fourier control scheme can fail as well. For rolls above $I_p \approx 130\ \mu\mathrm{W/cm^2}$, the control strength had to be increased to $s=0.6$, to prevent a transformation into spot patterns. Moreover, unlike in the experiment we do not observe a transition from hexagons to rolls for strong pump values. The transition can however, be observed numerically, when the boundary is included in the simulation. This highlights the influence of boundaries on the selection of patterns.

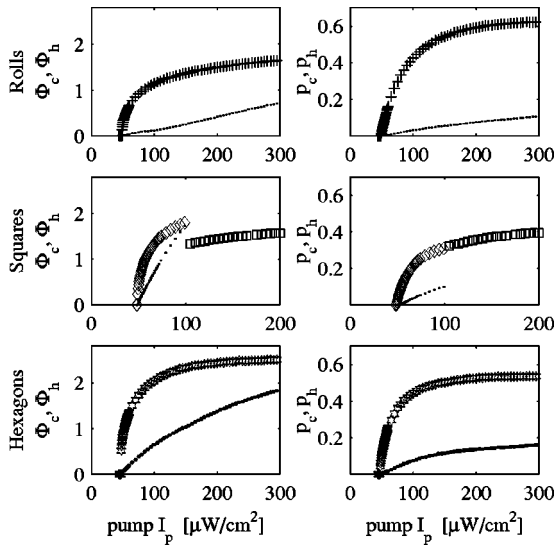

FIG. 5. Numerically determined total phase amplitudes (lhs column), and relative optical power (rhs column) in the critical wave number $0.8k_c<k<1.2k_c$ (large markers), and in the higher harmonics $1.2k_c<k$ (dots).

Pure square patterns are particularly difficult to stabilize. As in the experiments, there is a strong tendency to form sheared squares. Depending on the diameter of the spots of the control mask, shearing is to a certain amount compatible with the target state. We have here considered the slightly sheared squares in order to be in accordance with the experiment. For illustration, the amplitudes of pure squares ($\square$ markers, sheared squares have $\diamond$ markers) are shown in Fig. 5 as well. Pure squares could only stabilize far from the threshold with a larger control strength of $s=0.6$; we were not able to observe them close to the threshold. It is remarkable that pure and sheared squares differ considerably in their phase amplitude Φ_c, while the optical powers p_c are almost identical.

As before, we find a saturation of all amplitudes in the critical mode, accompanied by a growth of harmonics. The harmonics are particularly strong in the square patterns, mainly through the contribution of the first mixed harmonics at $k=\sqrt{2}k_c$. This finding can be explained by the close second unstable wave number $k_c^{(2)}$, promoting this harmonic mode.

In contrast to the experiment, from the simulations we can access the phase amplitude in absolute values. From there, we now see that the amplitudes asymptotically approach the maxima of the theoretical diffraction efficiencies, as derived in the Appendix (cf. Fig. 11). This makes sense, as a further increase in phase amplitude would lead to a decrease of the corresponding optical power in the critical mode—which in turn would have to lead to a decrease in phase amplitude. The interesting point is that, even though the calculation in the Appendix neglects harmonics and higher unstable wave numbers, it seems to hold surprisingly well far above threshold.

In Fig. 6, the numerical data points close to threshold are shown together with quadratic fits. The closeup reveals that, indeed, hexagons bifurcate subcritically, but with a very

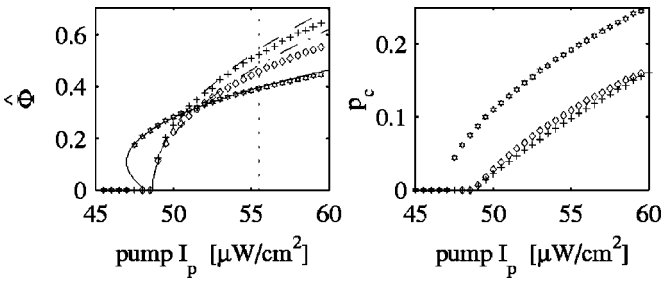

FIG. 6. Left hand panel: numerically determined phase amplitudes $\hat{\Phi}$ together with fits (+ and - -, rolls; ◇ and - · - , squares; ☆ and — , hexagons). The upper limit of the fit range is indicated by the vertical line. Right hand panel: corresponding optical power close to threshold.

small hysteresis. The results for the rolls and squares are in good agreement with the hypothesis that these solutions develop from a normal bifurcation.

The fit results in the following coefficients:

	a	b	a'	b'
Rolls	26.9	−1.21	0.553	−0.024
Squares	35.5	−1.74	0.73	−0.036
Hexagons	103.4	−22.5	2.15	−0.468

Again, the coefficients a, b are given in μW/cm^2.

For this fit, the threshold I_{th} has not been varied, since the normally bifurcating solutions indeed start at the theoretical threshold within the numerical error. Also, the coefficient $H=0$ was fixed to be zero, because the simulations do not contain imperfections. However, even when I_{th} and H are left as free fit parameters, the resulting coefficients a, b do not change significantly and I_{th} and H are very close to the expected values. Again, the fit result depends somewhat on the chosen interval, since the quadratic approximation in Eq. (4) is valid only close to threshold.

As in the experimental finding, the hexagonal solution bifurcates subcritically ($b<0$), and rolls and squares can be assumed to bifurcate normally ($b\approx 0$), as predicted by the theory. Actually, the values of b are small, but do not really vanish (and are even larger than those in the experiment). The explanation is that the numerical simulations have not always reached the perfect stationary state. For practical reasons, our convergence criterium had to be to put a small limit for the average phase change in each integration step. However, particularly close to threshold, slowing down phenomena can make the corresponding time constants very large and consequently the changes in each integration step extremely small, requiring excessive integration times. In the numerical runs, the pump intensity was decreased stepwise starting from a large value, so that the computed phase amplitudes are somewhat larger than the ideal asymptotic values. This results in a corresponding small upward shift of the fitted parabola.

Within these reservations, the agreement with the predictions of the Kerr model (7) is relatively good. However, we find the coefficient a' for the hexagons to be significantly larger than that expected in their approximation.

In the experimental measurement, the range of the existence of the hexagons starts about 1% below threshold with a finite amplitude of $\hat{\Phi}=0.07$. This compares quite well with the numerical results, namely $\hat{\Phi}=0.11$ at 2.5% below threshold. The agreement of the coefficients a and b between experiment and simulations proves to be satisfactory.

Finally, the plot in Fig. 6 also illustrates that the phase amplitude $\hat{\Phi}$ is a better choice as variable for the derivation of an amplitude equation. In contrast, the more linear dependence $p_c(I_p)$ is less well approximated by a square-root function. The relations (A4), (A7), and (A13) already state that, close to threshold, a square-root dependence of $\hat{\Phi}\sim\sqrt{I_p}$ corresponds to a linear dependence $p_c\sim I_p$. The absolute optical power would then be an even worse choice, as it grows quadratically with pump intensity $P_c\sim p_c I_p\sim I_p^2$.

V. SPATIAL INHOMOGENEITIES

It is well known that spatial perturbations can cause imperfect bifurcations and may lead to a shift of the pattern formation threshold [1]. However, the precise effect of a particular spatial perturbation is hard to predict beforehand. In our system, we identify three main candidates: inhomogeneities of the nonlinearity, speckles and the presence of boundaries. Numerical simulations allow one to investigate their respective influence separately. In the following, we will include each of the above inhomogeneities in a simulation of the system under Fourier control with hexagons as target state. The intention is to qualitatively identify the main cause of the imperfect bifurcations, rather than to exactly reproduce the experimental results, which would include too many unknown parameters.

A. Inhomogeneous nonlinearity

Our first assumption was that a slight inhomogeneity in the nonlinearity was the reason for the experimentally observed imperfect bifurcation. The thicknesses of the different layers of the LCLV can vary over the active area. In particular, the fabrication of a planar photoconductor layer is difficult. The effect is that the nonlinear transfer function $S(I_w)$ in Eq. (2), and, as consequence, also the pattern formation threshold, become space dependent.

On increasing the pump intensity from below threshold, the pattern starts to grow locally, where the local threshold is exceeded first. Under further increase of pump power, the pattern fills the active area. This effect is actually observed in the experiment, a snapshot of a pattern close to threshold is shown in Fig. 7.

Since the pattern amplitude is determined globally, namely, as amplitudes of the corresponding modes in the Fourier plane, the described gradual spreading of the pattern should result in a smooth growth of the pattern amplitude and thus can be responsible for an imperfect bifurcation.

The inhomogeneous nonlinearity was included in the numerical simulations by replacing $\Phi_{\max}\rightarrow[1+\chi(x,y)]\Phi_{\max}$ in Eq. (2). The inhomogeneity is small $|\chi(x,y)|<1$, with a vanishing average $\langle\chi\rangle_{x,y}=0$. Since we suppose that it has a

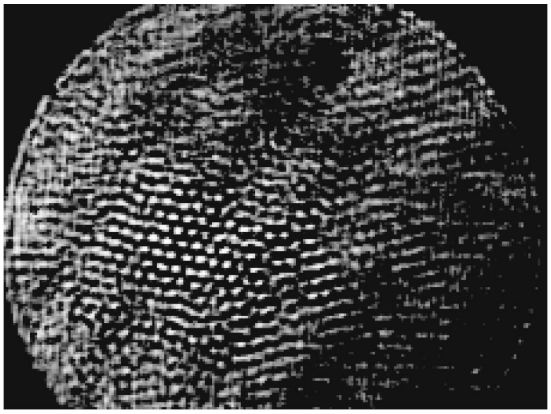

FIG. 7. Experimental snapshot of a pattern close to threshold, without control. The hexagonal pattern starts to grow locally, where the nonlinearity is most sensitive.

smooth profile, it is composed of small wave numbers with random phases. The distribution $\chi(x,y)$ used in the following is shown in Fig. 8.

A number of simulations were run varying the strength of the inhomogeneity, characterized by its standard deviation std(χ). As Fig. 8 shows, the inhomogeneity in the nonlinearity indeed causes a local growth of the pattern, corresponding to the experimental observation.

However, the resulting bifurcation diagrams do not show a significant deviation from the perfect bifurcation (Fig. 8). An increase of the strength of the inhomogeneity beyond std(χ)$>$0.3 provokes dynamics and disorder and a failure of

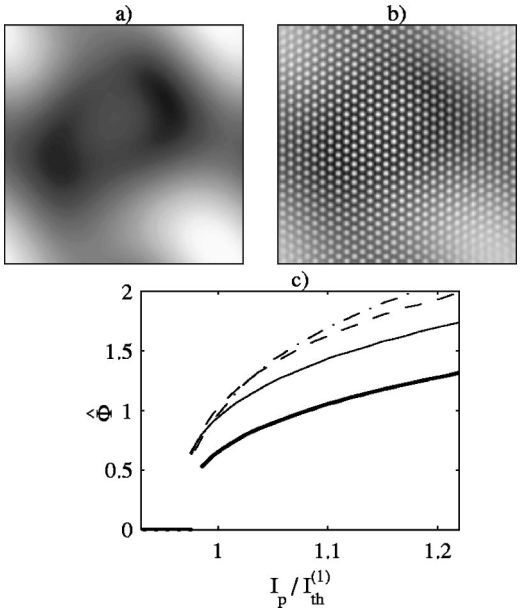

FIG. 8. Inhomogeneous nonlinearity: the upper left panel (a) shows the distribution of the inhomogeneity $\chi(x,y)$ used in the simulations. In the upper right panel (b), a typical resulting pattern under Fourier control close to threshold is presented. The resulting bifurcation diagram is shown in the lower panel (c). The parameter is the strength std(χ)$=$0.1 (solid), $=$0.2 (dashed), and $=$0.3 (dash dotted) of the inhomogeneity. The bold line gives the reference for the homogeneous case.

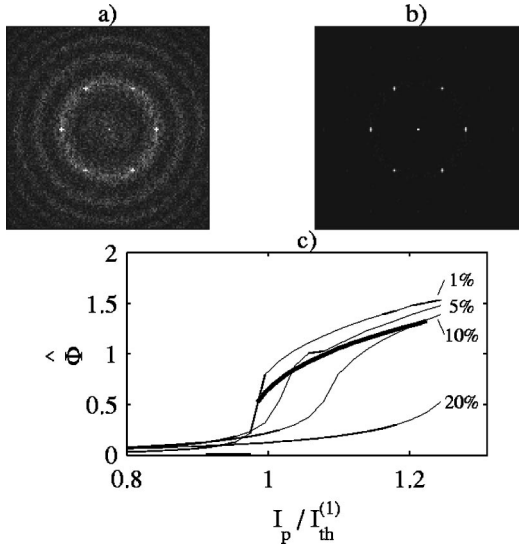

FIG. 9. Effect of speckles. Upper panels: far field 5% (a) and 15% above threshold (b). Lower graph (c): corresponding bifurcation diagrams; the parameter is the fraction f of the optical pump power in the speckles. The bold line again is the reference of the homogeneous case.

the control scheme. Consequently, the real inhomogeneity should be smaller, since this has not been observed experimentally.

B. Speckles

The second possible cause for the imperfect bifurcations is the scattering in the experimental setup. Small imperfections of the optical components, dust particles, minimal scratches, and also thermal fluctuations in the liquid crystal layer scatter part of the pump beam. This leads to speckles, i.e., broadband spatial noise. Even though in the experiment care had been taken to avoid scattering, speckles can never be disregarded completely.

Numerically, the speckles have been included as steady state, spatial white noise added to the pump wave $E_p \rightarrow E_p[1+\xi(x,y)]$, with ξ being complex. The phase and amplitude of this noise has been chosen such that a given fraction f of the total pump power is carried in nonzero Fourier modes at $\vec{k} \neq 0$.

In the simulations one can clearly observe, how, close to threshold, the system amplifies those noise contributions, which are near unstable wave numbers. Around threshold, the critical circles are broadly excited. Further above the threshold, this broad excitation collapses to the six hexagon target modes (Fig. 9).

The resulting bifurcation diagrams are shown in the lower panel of Fig. 9 with the noise amplitude f as parameter. Already a small amount of speckles clearly causes an imperfect bifurcation and leads to a shift of the threshold. Note that, for instance, a fraction of $f=5\%$ corresponds to a very small speckle intensity. The grid point representing the zero order mode in the Fourier plane carries a fraction $(1-f)=0.95$, whereas each of the remaining $N=(256^2-1)$ grid points carries in average a fraction of only $f/N<10^{-6}$ of the pump

power. However, close to threshold, noise near the critical wave numbers is substantially amplified.

This amplified noise contributes to the pattern modes, leading to a nonzero pattern amplitude already below threshold and thus causing an imperfect bifurcation. Moreover, the inhomogeneous pump profile induces a noisy phase profile, which again scatters part of the pump wave into random modes. This effectively wastes pump power and therefore leads to an increase of the pattern threshold.

C. Boundary

Finally, we consider the boundary of the active area, which—at least in the experiment—represents an unavoidable spatial inhomogeneity. Boundaries are also known to induce imperfect bifurcations and to shift threshold [1]. However, for the given aspect ratio of larger than 25, we had expected that the influence of the boundary would be small. Experimentally, the boundary is determined by the circular aperture $P2$ (cf. Fig. 1). This aperture is located in a plane which—due to the imaging by the lenses—is equivalent to the LCLV write side. Consequently, the write intensity I_w is forced to vanish outside the diameter of the aperture.

This kind of boundary has also been included in a numerical simulation. To be even more realistic, the shape of the pump beam has been considered in an additional simulation. While in the other simulations, the pump beam is assumed to be a plane wave, in the experimental reality it is an expanded Gaussian beam with a diameter of around 3 cm. Hence, across the diameter of the aperture, the variation in the pump intensity is in fact small.

These simulations reveal that the influence of the boundary is indeed quite strong. The fact that the pump beam is not exactly a plane wave also does have an effect, but much less than the mere presence of the boundary. The reason for the strong influence of the boundary is visualized by linear cuts through the pattern, as shown in Fig. 10. The pattern starts to grow in the center, its amplitude significantly decays towards the boundary.

The reason becomes clearer in a simple picture, when we remember the role of the Talbot effect in the pattern formation process: Due to this long-range (diffractional) coupling, each individual bright spot is supported by the presence of (regularly arranged) spots in the neighborhood. These surrounding spots are missing at the boundary.

The spatial range of this effect is rather large. Only with increasing pump intensity, the spots more and more gain a similar amplitude. The fact that the pattern does not have a uniform amplitude explains the smooth onset, i.e., the imperfect bifurcation.

The Fourier control, applied in all of the above cases, can lead to an additional shift of the observed threshold. The boundary introduces a large space scale and hence leads to a broadening of all modes [10,11]. Depending on the size of the spots on the Fourier mask, which block the target modes, outer parts of these broadened modes are suppressed. In particular, this concerns the zero mode, reducing the effective pump power. However, this effect is hard to estimate since it is not obvious to which extent modes can be broadened and still positively contribute to the pattern formation process. From our simulations we find that the corresponding increase in the observed threshold is less than 5%.

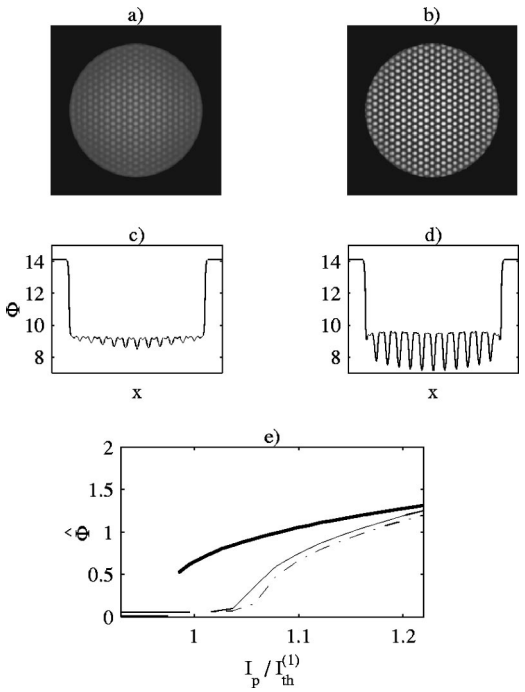

FIG. 10. Effect of a circular boundary. Upper panels: patterns 0.05% below threshold (a) and 23% above threshold (b). Linear cuts through the images (c),(d) demonstrate the decay of the pattern amplitude near the boundary. Lower graph (e): corresponding bifurcation diagram without (solid line) and with (dash-dotted line) inclusion of the Gaussian pump profile. The bold line again is the reference of the homogeneous case.

With respect to the different shifts in the threshold, the discrepancy between the theoretical and experimentally observed thresholds is, in fact, smaller than it seemed at first sight.

VI. CONCLUSION

We have demonstrated that the Fourier space control scheme is a valuable tool to access unstable regular solutions in spontaneous pattern formation. The properties of Fourier optics and the superposition principal of light waves make optical systems excellently suited for an implementation of this scheme. In contrast to a number of previous approaches, the control is spatially continuous and not restricted to a few local sites.

By stabilizing and tracking the generic, regular pattern solutions under variation of the stress parameter, an experimental bifurcation diagram was determined in an optical single-feedback system. The observed bifurcations are imperfect, which at first sight hides the behavior close to threshold. However, by fitting the theoretical dependence, as given by a prototype amplitude equation, it was possible to retrieve the bifurcation characteristics. The application of the Fourier space control also allowed us to go far above the threshold, where a saturation of the pattern amplitudes was

observed, accompanied by the growth of harmonics and higher wave numbers.

For comparison, numerical simulations of the full model were carried out. The experimental thresholds are in good agreement as well with the simulations as with the linear stability analysis of the model. Both numerics and experiment show that the hexagons bifurcate subcritically, but with a small hysteresis, as predicted by amplitude equations for a simpler model. The fitted coefficients of the amplitude equation are in reasonable agreement between experiment and numerics.

More detailed simulations revealed that the boundary and also the presence of speckles, experimentally caused by scattering in the setup, cause an imperfect bifurcation. Both mechanisms are also observed to cause an increase in the pattern formation threshold. In contrast to a first assumption, the role of inhomogeneities in the nonlinearity itself is obviously very small. The influence of the boundary and scattering is much stronger than expected in the first place. Even weak broadband spatial noise in the form of speckles has a considerable effect. From our findings we conclude that an experimental determination of the perfect bifurcation diagram would demand extreme aspect ratios and the absence of any sources of spatial noise.

ACKNOWLEDGMENTS

This work was supported by the German Science Foundation DFG (SFB 185) and by the Federal Ministry of Education and Research BMBF (Grant No. 13N7311-8). The authors particularly thank T. Tschudi for making this work possible. The authors also strongly benefited from an exchange with the University of Strathclyde, Glasgow, UK, as supported by the DAAD and the British Council (program ARC). We especially acknowledge the collaboration with G.-L. Oppo and G. K. Harkness. F. Kaiser and H. Sauermann have contributed very helpful discussions. Finally, we are very grateful for technical support by G. Jordan, D. Columbus, and our department's micro-optics group.

APPENDIX: PHASE AND INTENSITY AMPLITUDES

In the following, we will establish the relation between spatially periodic phase distributions and the corresponding power spectra. This gives the connection between the amplitude of the spontaneously formed phase patterns and the spectral intensity distribution. This problem is equivalent to the derivation of diffraction efficiencies of two-dimensional phase gratings, a typical problem in Fourier optics [21].

We will consider the three prototypes of periodic phase distributions, determined by a single wave number k_c, namely roll, square, and hexagon profiles,

$$\Phi=\hat{\Phi}\sum_{n=1}^{N}\cos(\vec{k}_n\vec{r}+\psi_n),\quad \vec{k}_n=k_c\begin{pmatrix}\cos(2n\pi/N)\\ \sin(2n\pi/N)\end{pmatrix} \tag{A1}$$

with $N=1,2,3$ respectively, and a phase amplitude $\hat{\Phi}$.

We start with the simplest case of a roll pattern ($N=1$): $\Phi^{(r)}=\hat{\Phi}^{(r)}\cos(\vec{k}_1\vec{r})$. In this case, the spatial phase ψ can be omitted, since it just represents a spatial shift in the plane $\vec{r}=(x,y)$ and corresponds to the choice of the origin. We now have to determine the Fourier spectrum of a wave $E=E_p\exp(-i\Phi)$ with the above phase distribution. The field can be rewritten as (Neumann) series over Bessel functions of the first kind

$$\begin{aligned}E^{(r)}&=E_p\exp[-i\hat{\Phi}^{(r)}\cos(\vec{k}_1\vec{r})]\\&=E_p\sum_{n=-\infty}^{\infty}(-i)^n\exp(in\vec{k}_1\vec{r})J_n(\hat{\Phi}^{(r)}).\end{aligned} \tag{A2}$$

Clearly, there are only discrete Fourier modes at $\vec{k}=n\vec{k}_1$ with relative amplitudes of

$$\eta_n^{(r)}\equiv\frac{E^{(r)}(\vec{k}=n\vec{k}_1)}{E_p}=(-i)^nJ_n(\hat{\Phi}^{(r)}). \tag{A3}$$

In the context of diffraction at phase gratings, η is the *diffraction efficiency*.

The intensity in the first order is proportional to the modulus square of the field amplitude,

$$|\eta_1^{(r)}|^2=\frac{|E^{(r)}|^2}{|E_p|^2}=J_1^2(\hat{\Phi}^{(r)})\approx\frac{\hat{\Phi}^{(r)2}}{4}, \tag{A4}$$

a result which is well known in Fourier optics [21].

The proceeding for a square phase pattern

$$\Phi^{(s)}=\hat{\Phi}^{(s)}[\cos(\vec{k}_1\vec{r})+\cos(\vec{k}_2\vec{r})] \tag{A5}$$

is similarly simple, since the two involved Fourier modes $\vec{k}_1\perp\vec{k}_2$ are perpendicular to each other. As before, the phases ψ_n can be omitted. Again, the phase modulated field is expanded in a Bessel series from which we derive the diffraction efficiency $\eta_{\mathrm{m,n}}^{(s)}$ for a Fourier mode at $\vec{k}=m\vec{k}_1+n\vec{k}_1$,

$$\eta_{\mathrm{m,n}}^{(s)}=(-i)^{m+n}J_m(\hat{\Phi}^{(r)})J_n(\hat{\Phi}^{(r)}). \tag{A6}$$

This leads to a relative intensity in a first order mode ($|m|=1,\quad n=0$ or $m=0,\quad |n|=1$) of

$$|\eta_1^{(s)}|^2=\frac{|E^{(s)}|^2}{|E_p|^2}=J_0^2(\hat{\Phi}^{(s)})J_1^2(\hat{\Phi}^{(s)})\approx\frac{\hat{\Phi}^{(s)^2}}{4}. \tag{A7}$$

The case of the hexagonal phase distribution

$$\Phi^{(h)}=\hat{\Phi}^{(h)}[\cos(\vec{k}_1\vec{r}+\psi_1)+\cos(\vec{k}_2\vec{r}+\psi_2)+\cos(\vec{k}_3\vec{r}+\psi_3)] \tag{A8}$$

with $\vec{k}_1+\vec{k}_2+\vec{k}_3=0$ is much less straightforward. First, we cannot omit the phases ψ_n here, since we have only two degrees of freedom in the choice of the coordinate origin. In practice, there are only two cases of interest which are characterized by maximal peak-to-peak phase amplitudes,

$\sum_{n=1}^{3} \psi_n = 0$: *positive* hexagons with phase peaks, or

$\sum_{n=1}^{3} \psi_n = \pi$: *negative* hexagons with phase dips (*honeycombs*).

We can retain a single phase $\psi = \psi_n = 0$, or $= \pi/3$, respectively.

The second problem arises from the fact that the three modes are not independent. This becomes clear in the expansion of the field

$$\begin{aligned} E^{(h)} &= E_p \exp[-i\hat{\Phi}^{(h)} \cos(\vec{k}_1 \vec{r})] \exp[-i\hat{\Phi}^{(h)} \cos(\vec{k}_2 \vec{r})] \\ &\quad \times \exp[-i\hat{\Phi}^{(h)} \cos(\vec{k}_3 \vec{r})] \\ &= E_p \sum_{l,m,n=-\infty}^{\infty} (-i)^{l+m+n} J_l(\hat{\Phi}^{(r)}) J_m(\hat{\Phi}^{(r)}) \\ &\quad \times J_n(\hat{\Phi}^{(r)}) \exp[i(l\vec{k}_1 + m\vec{k}_2 + n\vec{k}_3)\vec{r}] \\ &\quad \times \exp[i(l+m+n)\psi]. \end{aligned} \tag{A9}$$

Again, we find discrete Fourier modes, but now the amplitudes of each depend on an infinite set of possible linear combinations $\vec{k}_{\mathrm{lmn}} = l\vec{k}_1 + m\vec{k}_2 + n\vec{k}_3$.

We will focus on the first order modes, where the linear combinations result in one of the constituent modes $\vec{k}_{\mathrm{lmn}} = \vec{k}_1$. This mode results from all wave vector combinations which fulfill $m = n = l - 1$. Inserting this condition into Eq. (A9), we get

$$\begin{aligned} \eta_1^{(h)} &= \frac{E^{(h)}(\vec{k} = \vec{k}_1)}{E_p} \\ &= \sum_{m=-\infty}^{\infty} (-i)^{-m+1} J_m^2(\hat{\Phi}^{(h)}) J_{m+1}(\hat{\Phi}^{(h)}) e^{i(3m+1)\psi}. \end{aligned} \tag{A10}$$

The expression can be rearranged for positive hexagons ($\psi = 0$) to

$$\begin{aligned} \eta_1^{(h+)} &= -iJ_0^2(\hat{\Phi}^{(h)}) J_1(\hat{\Phi}^{(h)}) \\ &\quad + \sum_{m=1}^{\infty} i^{m+1} J_m^2(\hat{\Phi}^{(h)}) [J_{m-1}(\hat{\Phi}^{(h)}) - J_{m+1}(\hat{\Phi}^{(h)})], \end{aligned} \tag{A11}$$

and for negative hexagons ($\psi = \pi/3$) to

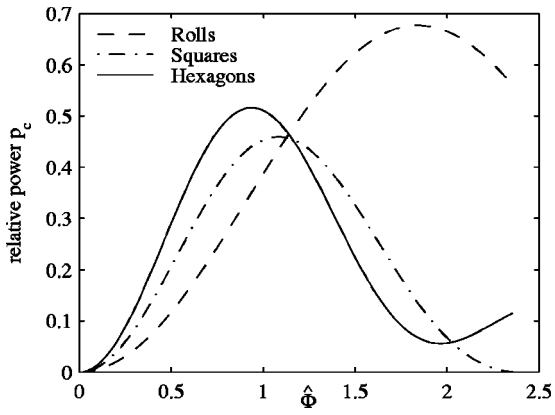

FIG. 11. Optical power p_c, relative to the incident power, in the first diffraction order of periodic phase distributions with roll, square, and hexagonal symmetry.

$$\begin{aligned} \eta_1^{(h-)} &= e^{i\pi/3} \Big\{ -iJ_0^2(\hat{\Phi}^{(h)}) J_1(\hat{\Phi}^{(h)}) \\ &\quad + \sum_{m=1}^{\infty} (-1)^m i^{m+1} J_m^2(\hat{\Phi}^{(h)}) \\ &\quad \times [J_{m-1}(\hat{\Phi}^{(h)}) - J_{m+1}(\hat{\Phi}^{(h)})] \Big\}. \end{aligned} \tag{A12}$$

The resulting relative intensities in the first order are identical for positive and negative hexagons and can be approximated by

$$\begin{aligned} |\eta_1^{(h)}|^2 &\approx J_0^4(\hat{\Phi}^{(h)}) J_1^2(\hat{\Phi}^{(h)}) + J_0^2(\hat{\Phi}^{(h)}) J_1^4(\hat{\Phi}^{(h)}) \\ &\approx \frac{\hat{\Phi}^{(h)2}}{4} \left(1 - \frac{\hat{\Phi}^{(h)2}}{4}\right)^2. \end{aligned} \tag{A13}$$

For the total power in the first order $P_c = P(|\vec{k}| = k_c)$, we have to consider the number of modes N,

$$p_c = \frac{P_c}{P_p} = 2N|\eta_1|^2 \tag{A14}$$

here scaled by the total optical power P_p of the incident wave. These relative powers $p_c(\hat{\Phi})$ are plotted in Fig. 11.

All curves have distinct maxima located at

$$\begin{aligned} p_c^{(r)}(\hat{\Phi} = 1.83) = 0.677, \quad p_c^{(s)}(\hat{\Phi} = 1.07) = 0.460, \\ p_c^{(h)}(\hat{\Phi} = 0.928) = 0.516. \end{aligned} \tag{A15}$$

The above calculations are based on the assumption in Eq. (A1) that the phase distribution $\Phi(\vec{r})$ contains only a single

wave number $|\vec{k}_n| = k_c$. In so far, the results are applicable to the spontaneously formed patterns until higher harmonics start to contribute significantly. The effects of higher harmonics are not simple to estimate. If they were independent of the basic modes considered so far, they would just decrease the available total intensity by diffracting it into other orders. The interaction between harmonic and basic modes can, however, lead to energy transfer in both directions.

[1] M. C. Cross and P. C. Hohenberg, Rev. Mod. Phys. **65**, 851 (1993); P. Manneville, *Dissipative Structure And Weak Turbulence* (Academic Press, San Diego, 1990).

[2] J. Opt. Soc. Am. B **7** (6/7) (1990), special issue on transverse effects in nonlinear-optical systems, edited by N. B. Abraham and W. J. Firth; F. T. Arecchi, Physica D **51**, 450 (1991); L. A. Lugiato, Phys. Rep. **219**, 293 (1992); C. O. Weiss, *ibid.* **219**, 311 (1992); *Nonlinear Dynamics and Spatial Complexity in Optical Systems*, edited by R. G. Harrison and J. S. Uppal (SUSSP Publications, Edinburgh, 1992); Chaos Solitons Fractals **4** (8/9) (1994), special issue on nonlinear optical structures, patterns, chaos, edited by L. A. Lugiato; L. A. Lugiato, M. Brambilla, and A. Gatti, Adv. At., Mol., Opt. Phys. **40**, 229 (1998); Chaos Solitons Fractals **10** (4/5) (1999), special issue on pattern formation in nonlinear optical systems, edited by R. Neubecker and T. Tschudi; F. T. Arecchi, S. Boccaletti, P.-L. Ramazza, Phys. Rep. **318**, 83 (1999).

[3] J. Tang and H. H. Bau, Phys. Rev. Lett. **70**, 1795 (1993); H. Gang and H. Kaifen, *ibid.* **71**, 3794 (1993); F. Qin, E. E. Wolf, and H. C. Chang, *ibid.* **72**, 1459 (1994); I. Aranson, H. Levine, and L. Tsimring, *ibid.* **72**, 2561 (1994); W. Lu and R. G. Harrison, Opt. Commun. **109**, 457 (1994); V. Petrov, S. Metens, P. Borckmans, G. Dewel, and K. Showalter, Phys. Rev. Lett. **75**, 2895 (1995); A. Hagberg, E. Meron, I. Rubinstein, and B. Zaltzman, *ibid.* **76**, 427 (1996); Th. Pierre, G. Bonhomme, and A. Atipo, *ibid.* **76**, 2290 (1996).

[4] V. Petrov, Q. Ouyang, and H. L. Swinney, Nature (London) **388**, 655 (1997); A. K. Horvath, M. Dolnik, A. P. Munuzuri, A. M. Zhabotinsky, and I. R. Epstein, Phys. Rev. Lett. **83**, 2950 (1999).

[5] P. Kolodner and G. Flätgen, Phys. Rev. E **61**, 2519 (2000).

[6] M. E. Bleich, D. Hochheiser, J. V. Moloney, and J. E. S. Socolar, Phys. Rev. E **55**, 2119 (1997).

[7] R. Martin, A. J. Scroggie, G.-L. Oppo, and W. J. Firth, Phys. Rev. Lett. **77**, 4007 (1996); G. K. Harkness, R. Martin, A. J. Scroggie, G.-L. Oppo, and W. J. Firth, Phys. Rev. A **58**, 2577 (1998); G. K. Harkness, G.-L. Oppo, E. Benkler, M. Kreuzer, R. Neubecker, and T. Tschudi, J. Opt. B: Quantum Semiclassical Opt. **1**, 177 (1999).

[8] A. V. Mamaev and M. Saffman, Phys. Rev. Lett. **80**, 3499 (1998); S. J. Jensen, M. Schwab, and C. Denz, *ibid.* **81**, 1614 (1998); Y. Hayasaki, H. Yamamoto, and N. Nishida, Opt. Commun. **187**, 49 (2001); E. V. Degtiarev and M. A. Vorontsov, J. Opt. Soc. Am. B **12**, 1238 (1995).

[9] T. Ackemann, B. Giese, B. Schäpers, and W. Lange, J. Opt. B **1**, 70 (1999).

[10] E. Benkler, M. Kreuzer, R. Neubecker, and T. Tschudi, Phys. Rev. Lett. **84**, 879 (2000).

[11] E. Benkler, M. Kreuzer, R. Neubecker, and T. Tschudi, J. Opt. A, Pure Appl. Opt. **2**, 303 (2000).

[12] Yu. D. Dumarevskii *et al.*, Kvant. Elektron. **11**, 730 (1989) [Sov. J. Quantum Electron. **14**, 493 (1984)]; *Spatial Light Modulator Technique*, edited by U. Efron (Marcel Dekker, New York, 1995); W. P. Bleha, Laser Focus/Electro Opt. **19**, 110 (1983), and references therein; N. Hawlitschek, P. Gärtner, P. Gussek, and F. Reichel, Exp. Tech. Phys. (Lemgo, Ger.) **40**, 199 (1994).

[13] W. H. F. Talbot, Philos. Mag. **9**, 401 (1836); E. Ciaramella, M. Tamburrini, and E. Santamato, Appl. Phys. Lett. **63**, 1604 (1993).

[14] W. J. Firth, J. Mod. Opt. **37**, 151 (1990); M. Le Berre, E. Ressayre, A. Tallet, and J.-J. Zondy, J. Opt. Soc. Am. B **7**, 1346 (1990); G. D'Alessandro and W. J. Firth, Phys. Rev. Lett. **66**, 2597 (1991); R. Macdonald and H. J. Eichler, Opt. Commun. **89**, 289 (1992); M. Tamburrini, M. Bonavita, S. Wabnitz, and E. Santamato, Opt. Lett. **18**, 855 (1993); M. A. Vorontsov and W. J. Firth, Phys. Rev. A **49**, 2891 (1994); G. Grynberg, A. Maître, and A. Petrossian, Phys. Rev. Lett. **72**, 2379 (1994); T. Ackemann, Y. A. Logvin, A. Heuer, and W. Lange, *ibid.* **75**, 3450 (1995); J. Glückstad and M. Saffman, Opt. Lett. **20**, 551 (1995); T. Honda and H. Matsumoto, *ibid.* **20**, 1755 (1995); T. Honda, H. Matsumoto, M. Sedlatschek, C. Denz, and T. Tschudi, Opt. Commun. **33**, 293 (1997).

[15] G. D'Alessandro and W. J. Firth, Phys. Rev. A **46**, 537 (1992).

[16] R. Neubecker, G.-L. Oppo, B. Thüring, and T. Tschudi, Phys. Rev. A **52**, 791 (1995); B. Thüring, R. Neubecker, M. Kreuzer, E. Benkler, and T. Tschudi, Asian J. Phys. **7**, 453 (1998).

[17] S. A. Akhmanov, M. A. Vorontsov, and V. Yu. Ivanov, Pis'ma Zh. Eksp. Teor. Fiz. **47**, 611 (1988) [JETP Lett. **47**, 707 (1988)]; S. A. Akhmanov *et al.*, J. Opt. Soc. Am. B **9**, 78 (1992); B. Thüring, R. Neubecker, and T. Tschudi, Opt. Commun. **102**, 111 (1993); E. Pampaloni, S. Residori, and F. T. Arecchi, Europhys. Lett. **24**, 647 (1993); M. A. Vorontsov and W. J. Firth, Phys. Rev. A **49**, 2891 (1994); E. Pampaloni, P.-L. Ramazza, S. Residori, and F. T. Arecchi, Phys. Rev. Lett. **74**, 258 (1995); B. Thüring, A. Schreiber, M. Kreuzer, and T. Tschudi, Physica D **96**, 282 (1996); A. Schreiber, B. Thüring, M. Kreuzer, and T. Tschudi, Opt. Commun. **136**, 415 (1997); Y. Hayasaki, H. Yamamoto, and N. Nishida, *ibid.* **151**, 263 (1998); F. T. Arecchi, S. Boccaletti, S. Ducci, E. Pampaloni, P.-L. Ramazza, and S. Residori, J. Nonlinear Opt. Phys. Mater. **9**, 183 (2000).

[18] R. Neubecker, B. Thüring, M. Kreuzer, and T. Tschudi, Chaos Solitons Fractals **10**, 681 (1999).

[19] The amplitude equation coefficients in Ref. [15] have to be taken close to threshold, i.e., in the expressions for η, ξ_1, and ξ_2 one has actually to set $p=1$, G. D'Alessandro (private communication).

[20] The simple linear fit, as peformed in a first attempt in Ref. [11] to determine the threshold, is actually not correct. The seemingly linear dependence is caused by the imperfect bifurcation, which at that time has not been considered in detail.

[21] J. W. Goodman, *Introduction to Fourier Optics* (McGraw-Hill, Singapore, 1996).